2026 IEEE/SICE International Symposium on System Integration (SII)
January 11-14, 2026. Cancún, México

Enhancing Vision-Based Tactile Sensing Through a Fingernail-Inspired Structure for Improved Contact and Texture Detection

Takeshi Tomomizu[1] and Van Anh Ho[1]

***Abstract*— Vision-based tactile sensors (VBTS) have demonstrated strong potential for high-resolution contact measurement, yet their structural design offers room for further improvement. In this study, we examine the impact of incorporating a human fingernail-inspired structure on the performance of VBTS in measuring contact areas and detecting fine textures. Tensile tests were conducted on four flexible skin materials, and VBTS units were fabricated both with the nail structure (w-VBTS) and without it (wo-VBTS) to evaluate contact areas on flat surfaces. Based on the tensile test results regarding durability and material transparency, the optimal skin material was selected for the w-VBTS, which was then used in fine step detection experiments. Our findings reveal that the nail structure effectively reduced excessive skin deformation and increased the contact area. Furthermore, fine texture detection at the nail tip was achieved with a maximum error of 0.69 mm. These results suggest that emulating the structural features of the human finger can enhance the performance of VBTS in robotic manipulation tasks.**

I. INTRODUCTION

Tactile sensing is essential for both humans and robots in recognizing objects and performing dexterous manipulation. Human hands have four main receptors: Meissner's corpuscles, Merkel's discs, Pacinian corpuscles, and Ruffini endings. Each detects different sensory signals and contributes to our rich sense of touch [1]. Similarly, robots also need tactile sensing to manipulate objects reliably and explore complex, dynamic environments. Various tactile sensors [2]–[5] have been extensively studied. In [3], the authors present a unified sensor module that detects temperature variations and contact cues, demonstrating its performance by grasping a plastic cup. In [4] proposed a capacitive sensor based on a flexible silver nanowire network electrode. In [5], the authors use MLX90393 Hall-effect sensors to detect the displacement of miniature magnets embedded in a silicone elastomer, convert those measurements into force vectors for tactile estimation, and evaluate its grasping performance via sequential response. However, many conventional tactile sensors suffer from robustness issues, have complex internal wiring that makes maintenance difficult, and exhibit limited spatial resolution. In recent years, many studies have investigated vision-based tactile sensors (VBTS) [6], [7]. VBTS equipped with internal cameras can capture high-resolution images of soft elastomer deformations caused by contact with an object. A typical VBTS consists of a flexible elastomeric layer that conforms to the object's shape upon contact, a camera placed beneath the elastomer to record its deformation, and an LED illumination system located between the elastomer and the camera to provide uniform lighting.

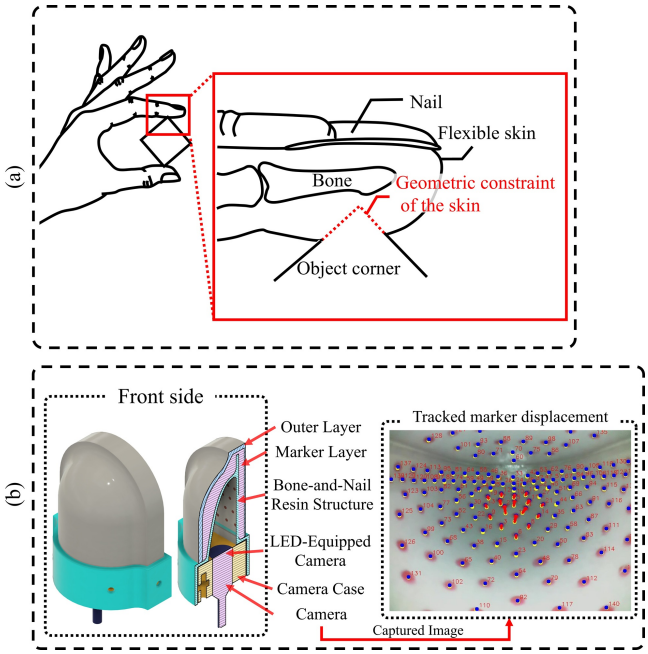

Fig. 1: Proposed VBTS: (a) Human finger structure with flexible skin geometric constraint; (b) Overview of the sensor design and marker displacement tracking

VBTS are typically divided into two categories, which are marker-based and reflective types. The former one, represented by *TacTip* type sensors [6], [8], [9], uses marker tracking within a flexible dome or flat shaped elastomer membrane to acquire tactile information through a simple sensor architecture with minimal wiring. Benjamin *et al.* [8], [9] demonstrated that integrating *TacTip* sensors into the Open Hand M2 and GR2 grippers, combined with model free Bayesian estimation of marker displacement data, enables high precision in-hand manipulation using tactile feedback alone. This approach allows accurate grasp pose estimation and active reorientation of cylindrical objects. However, in these systems the effective sensing area remains limited [8]–[10], which constrains their applicability to more dexterous object manipulation.

In contrast, reflective VBTS, such as GelSight type sensors [7], [11], [12] use colored internal illumination combined with photometric stereo analysis to reconstruct silicone skin deformations with micrometer scale resolution. Wang *et al.* [11] proposed that high precision tracking of two dimen-

[1]Authors are with Japan Advanced Institute of Science and Technology (JAIST), 1-1 Asahidai, Nomi, Ishikawa, 923-1292 Japan. Emails: s2320009@jaist.ac.jp, van-ho@jaist.ac.jp

978-1-6654-5784-2/26/$31.00 ©2026 IEEE

sional marker displacements enables quantitative measurement of subtle slip and shear deformations in the planar deformation field induced by contact, which are difficult to resolve with conventional photometric stereo analysis. Rayamane *et al.* [12] developed a robust GelSight type VBTS using a latex coated silicone elastomer that combines high load durability with elastic recovery, and demonstrated durability up to 50 N and more than 93% accuracy in spatial resolution. However, because all of these sensors are based on planar configurations, their capability for dexterous object manipulation is limited. More recently, Won *et al.* [13] and Zhou *et al.* [14] have reported systems that exploit a fingernail inspired structure to enable the manipulation of thin objects, which represents one of the functional capabilities of the human finger. Nevertheless, even in these designs, the tactile sensing region remains limited, and because the nail structure is implemented as an external attachment to the VBTS, tactile information is not in practice acquired at the nail region.

In contrast, the human finger has a multilayered structure (Fig. 1a) consisting of the nail, bone, and flexible skin. Among these components, the nail structure plays an important mechanical role by locally concentrating contact forces at the fingertip, which enables precise manipulation of small objects, facilitates scratching motions, and suppresses excessive deformation of the flexible skin to increase the contact area [15]–[17]. However, although the nail plays a critical role in fingertip mechanics, VBTS sensor designs have generally not incorporated biomimetic nail structures intended to mimic its mechanical function.

Therefore, this study proposes a novel marker based VBTS inspired by the human finger structure (Fig. 1b), referred to as the with-nail VBTS (w VBTS). In two experimental evaluations, we show that incorporating this biomimetic nail structure into VBTS increases the contact area and improves sensitivity to subtle surface features at the nail region.

The remainder of this paper is organized as follows: Section II provides an overview of related work; Section III describes the characterization results for five flexible materials and the fabrication process of the proposed VBTS; Section IV details the experimental setup and evaluation methods utilized for assessing contact area and fine steps detection; Section V presents the experimental results; and Section VI concludes the paper and outlines directions for future research.

II. RELATED WORK

A. Bioinspired Robotic Finger

In previous robotic fingertip designs, attention to the anatomical structure of the human finger has been shown to contribute to enhanced grasp stability [16], [18], the detection of subtle surface discontinuities, and the manipulation of thin objects. Controzzi *et al.* [16] developed a bio-inspired multilayer fingertip and showed via compression tests, 3D FEA (Finite Element Analysis), and grip test that it reproduces human-like mechanics and surpasses rigid steel alternatives in grasp stability. Kumagai *et al.* [18] demonstrated that

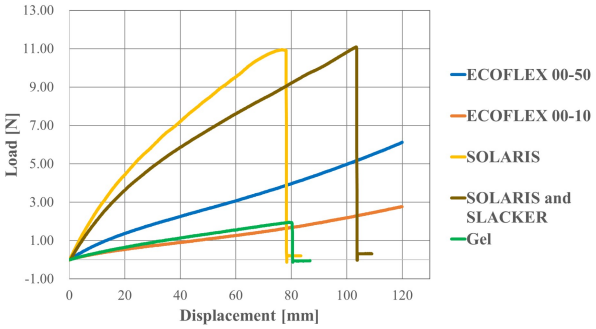

Fig. 2: Tensile tests results

artificial fingertips incorporating a bio-mimetic nail structure substantially improve pull-out durability, especially when paired with a soft elastomer skin. Murakami *et al.* [19] proposed a novel fingertip design that combines a flexible soft skin layer with a rigid nail. They demonstrated that this configuration integrates friction modulation, sub-millimeter step detection, and contact state recognition, enabling multifunctional grasp control.

B. Bioinspired VBTS

In the field of VBTS, a wide range of GelSight type sensor configurations has been proposed. Standard GelSight sensors feature a planar sensing area [7], which constrains their utility for object manipulation. To extend beyond their flat sensing region, Romero *et al.* [20] proposed an optical tactile sensor featuring a rounded fingertip geometry that captures flexible, high resolution 3D tactile information in real time. They validated its utility through manipulation experiments with a variety of objects. Gomes *et al.* [21] introduced a tactile sensor that employs the entire finger as its sensing region, enabling contact detection at any location. They experimentally demonstrated that the device can capture high-resolution contact data over the full finger surface, including both the tip and the sides. Moreover, several other GelSight type tactile sensors with whole-finger sensing capabilities have been reported [22], [23]. Andrussow *et al.* [22] proposed Minsight, a thumb-sized (22 mm diameter × 30 mm height) VBTS and demonstrated in evaluation experiments that it achieves an average positional error of 0.6 mm and a force error of 0.07 N, validating its high speed, compact, and practical tactile sensing performance. Azulay *et al.* [23] introduced AllSight, an optical tactile sensor that enables a model trained on one device to be applied to newly fabricated identical sensors without additional training and demonstrated zero-shot transfer with a position error of 3.49 mm, a force error of 2.06 N, and a torsion error of 0.0068 Nm in evaluation experiments.

To the best of our knowledge, there are no existing VBTS designed to mimic the human fingertip's multilayered structure of nail, bone, and flexible skin. Through experimental evaluation, we demonstrate that this biomimetic design markedly increases the contact area and enables the nail tip to detect fine periodic surface steps.

TABLE I: Mixing ratios and optical properties of the five flexible materials. (T: Transparent, O: Opaque)

No.	Material	Part A	Part B	Slacker	T or O
1	ECOFLEX 00–50	1	1	–	O
2	ECOFLEX 00–10	1	1	–	O
3	SORALIS	1	1	–	T
4	SORALIS and Slacker	1	1	0.5	T
5	Gel	1	1	–	T

III. MATERIALS AND FABRICATION

A. Materials evaluation

To select the soft skins for the proposed with and without nail VBTS (w/wo-VBTS), we evaluated the durability of five different materials through tensile tests. The materials were as follows: No. 1: Ecoflex 00-50 (Smooth-On Inc.), No. 2: Ecoflex 00-10 (Smooth-On Inc.), No. 3: Solaris (Smooth-On Inc.), No. 4: mixture of Solaris and Slacker (Smooth-On Inc.), and No. 5: Gel (hardness 7) (EXSEAL Co., Ltd.). The mixing ratios of each material are summarized in TABLE I, and a small amount of black or white pigment was added to each formulation to facilitate contact area analysis. Furthermore, the contact area comparison experiments w-VBTS and wo-VBTS were conducted using four materials (No. 1, 2, 4, and 5 in TABLE I) to examine changes in contact area due to the presence or absence of the nail structure. Material No. 3 was excluded because No. 4 offered greater durability and flexibility. Based on the tensile test results and the material's transparency, we selected the mixture listed as No. 4 in TABLE I for the w-VBTS skin used in our experiments to detect subtle surface features.

B. Fabrication

The fabrication method for the proposed w-VBTS is described below. The internal rigid structures of the w/wo-VBTS were 3D printed on a Form3+ stereo lithography printer using Clear Resin V4 (Fig. 3 (A)). The fabricated parts are polished with sponge polishing pads and polishing compounds to produce transparent rigid structure. In Fig. 3 (A) shows the integrated nail and bone transparent structure on the left and the bone only transparent structure on the right side.

Next, the skins for both w-VBTS and wo-VBTS are formed using a mold casting process (Fig. 3 (B)). The wo-VBTS fabrication process is identical except for the use of a different mold, and is therefore omitted here. In addition, although the skin fabrication process presented in this chapter is exemplified using a blend of Solaris and Slacker, it can also be applied when using other materials. First, the transparent rigid structure is placed in the marker layer mold and the material was injected (Fig. 3 (B-1)). After the material cures, the molded part is carefully demolded. The marker layer mold's protrusions generated groove features on the surface of the cured marker layer skin. We manually filled the grooves with silicone blend of Solaris and Slacker, colored with red pigment (Smooth-On Inc.) to create the markers (Fig. 3 (B-2)). Next, the rigid component with

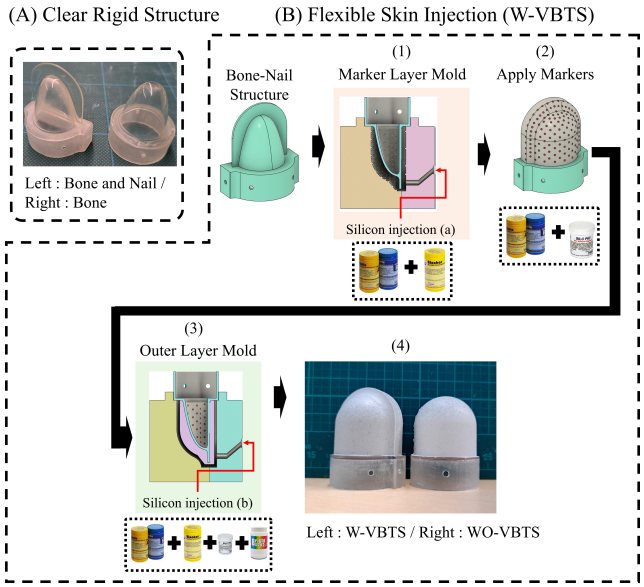

Fig. 3: Fabrication process of fingertip: (A) Step by step polishing of the clear rigid structure; (B) Process of skin fabrication

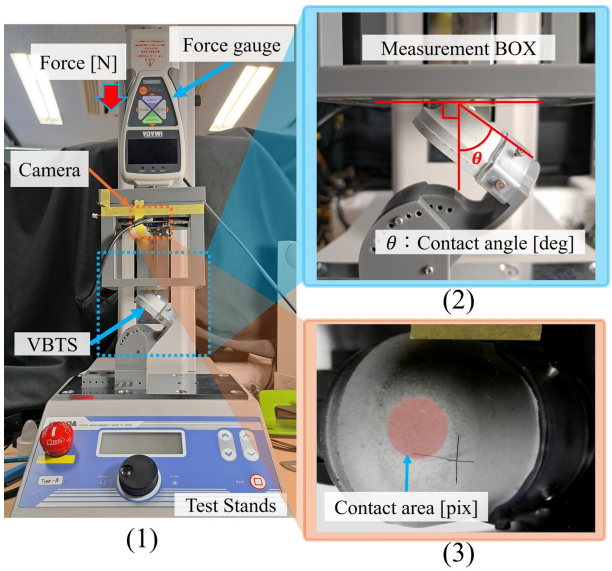

Fig. 4: Contact area measurement setup

the completed marker layer was placed in the outer layer mold, and a silicone blend of Solaris and Slacker, colored with white pigment (Smooth-On Inc.) and black pigment (Komatsu Process Co., Ltd.), was injected (Fig. 3 (B-3)). After curing, the rigid component is carefully demolded, and the excess skin trimmed away to obtain the integrated skin and rigid structure of the proposed w/wo-VBTS (Fig. 3 (B-4)). Finally, the module combining flexible skin and rigid structure is integrated with the camera (SYD-V31105L-158A-01,MISUMI Electronics Corp.) and its housing (Fig. 1 (b)), completing the proposed w/wo-VBTS sensors.

IV. EXPERIMENTAL SETUP

In this paper, we aim to enhance the contact area detection and texture discrimination ability of the proposed design. In this section, we introduce experiment setups and related methods.

A. Contact area comparison

1) Experimental environment

The experimental setup for the contact area comparison experiment is illustrated in Fig. 4, where the proposed w/wo-VBTS was mounted on a test stand (MX2-500N, Imada Co., Ltd.). A force gauge (ZTA 50N, Imada Co., Ltd.) was mounted on the sliding section of the test stand. A measurement box (MB), equipped with an camera (ELP-USB8MP04AF-V72) and an acrylic plate, was attached to the tip of the force gauge (Fig. 4-1). By adjusting the mounting fixture, the contact angle θ of the w/wo-VBTS relative to the MB can be controlled (Fig. 4-2). The MB moved downward at a constant speed of 15 mm/min. When the force gauge reading reached 5 N, the motion stopped and the internal camera captured images of the contact surface. We performed ten trials at each of three contact angles (50°, 60°, and 70°). w/wo-VBTS sensors fabricated from the four materials (No. 1, No. 2, No. 4, and No. 5) listed in TABLE I were evaluated for comparison.

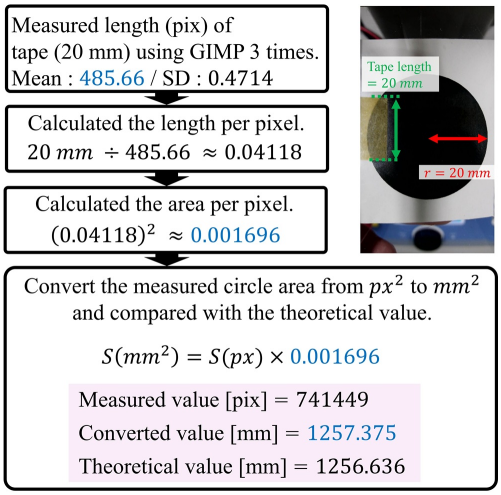

Fig. 5: Derivation process of the pixel-to-millimeter conversion formula using reference tape measurement and circular area calculation.

2) Contact surface image analysis

The images captured by the MB's internal camera were manually analyzed in GIMP (GNU Image Manipulation Program) to measure the contact area (Fig. 4-3). Pixel based contact area values from GIMP were converted to mm² using equation (1). The derivation process of equation (1) is shown in Fig. 5. First, a masking tape with a length of 20 mm and a printed circle with a radius of 20 mm were attached to the acrylic plate of the MB. The length of the tape was measured three times using GIMP, and the results were an average of 485.66 pixels and a standard deviation of 0.4714 pixels. From these measurements, the pixel value per mm^2 was calculated to be 0.001696, which was then used as the conversion coefficient in equation (1). For validation, the area of the circle with a radius of 20 mm was computed, and the difference from the theoretical value was approximately 0.73 mm^2, indicating that this conversion method is suitable for utilization in the present experiment.

$$S_{\mathrm{mm^2}} = S_{\mathrm{pix}} \times 0.001696 \tag{1}$$

3) Statical analysis

We assessed normality of the contact area data for each material, angle, and condition using the Shapiro Wilk test at α = 0.05. When normality was not rejected we applied Welch's t test. When normality was rejected we applied the nonparametric Mann Whitney U test. All tests were two sided. To control for multiple comparisons we used the Bonferroni correction. The family wise significance level was α = 0.05 and the number of comparisons was $m = 12$ based on four materials and three contact angles. The adjusted threshold was $\alpha^* = 0.05 \,/\, 12 = 0.00417$.

B. Nail tip step detection experiment

1) Experimental environment

In this experiment, the objective is to evaluate the capability of the w-VBTS fingertip to detect the frequency characteristics of surface patterns, using four types of samples with equally spaced triangular patterns (Fig. 6, d = 8, 4, 2, and 1 mm). The fingertip skin was made from a mixture of Solaris and Slacker to ensure transparency (TABLE I) and durability (Fig. 2). A force-torque sensor (FT300-S, Robotiq Inc.) was mounted on an X-axis linear stage (KXL06300-C2-F2A, Suruga Seiki Co., Ltd.). A specimen (Sp) with a triangular, evenly spaced asperity pattern was placed on the top surface of the force-torque sensor (Fig. 6). Next, the w-VBTS was mounted at the tip of a simple finger assembled from two servomotors (XM430-W350, Robotis Co., Ltd.). The servo angle was set ($\theta_1 = 260°$, $\theta_2 = 90°$) so that the fingernail tip contacted the surface ridges of the Sp, and the linear stage moved in the $+X$ direction at 2 mm/s. For the experiment with the wo-VBTS, the servo angles were set to ($\theta_1 = 258°$, $\theta_2 = 94°$). During this movement, the sensor recorded forces and torques along the X, Y, and Z axes, while the w-VBTS internal the camera simultaneously captured marker displacements.

2) Marker tracking and quantification methods

The system first detects the marker positions $\{p_i^0\}$ in the reference image using YOLOv8 [24]. Here, i denotes the marker index. It then sorts the markers by their polar coordinates with respect to the frame center and assigns ID numbers in counterclockwise order, starting from the center outward. The marker tracking at each frame t is carried out in two steps. First, a cost matrix from equation (2) is generated using the previous frame's tracking positions $\{p_i^{t-1}\}$ and the YOLOv8 detection positions $\{d_j^t\}$, and the $Hungarian$ algorithm is used to find the optimal matches.

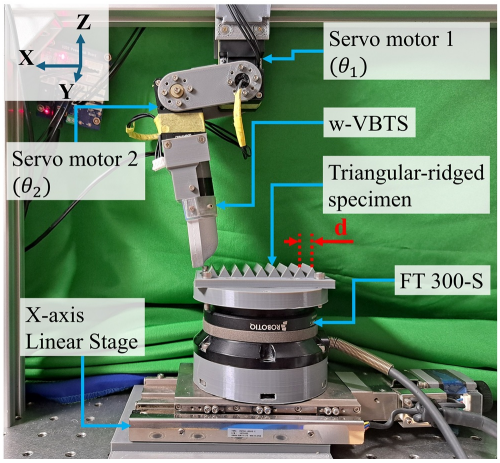

Fig. 6: Setup for fine step detection experiment using the w-VBTS, triangular ridged specimen (pitch d), FT 300-S sensor, and X-axis stage.

$$G_{ij} = \|p_i^{(t-1)} - d_j^t\| \tag{2}$$

Second, any matched pair with a distance below the threshold (20 pixels in this study) is treated as the same marker, and the tracking positions $\{p_i^t\}$ are updated accordingly. In equation (2), $\|\cdot\|$ denotes the Euclidean norm. Next, the displacement vector Δp_i^t from the initial position is calculated for each marker using equation (3). Only those vectors the magnitude $\|\Delta p_i^t\|$ of which exceeds the threshold $\delta = 3$ pix are summed, and the combined displacement vector is obtained via equation (4). The combined displacement vector, along with its timestamp, was recorded in a CSV file.

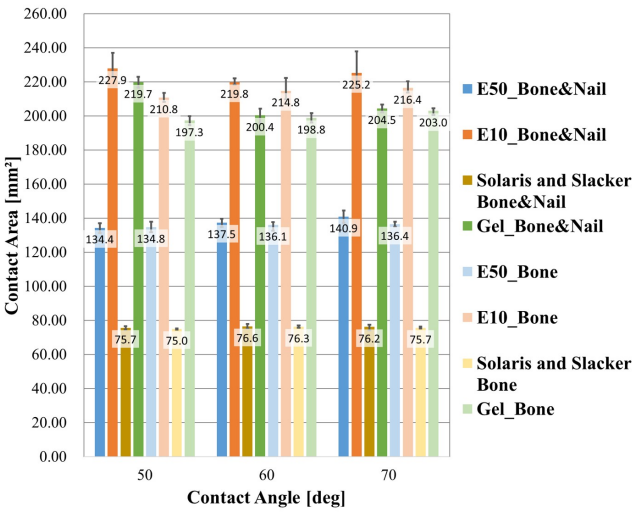

Fig. 7: Comparison of contact areas between VBTSs with and without nail structure using four types of flexible skin materials (E50, E10, Solaris and Slacker, Gel) at different contact angles (50°, 60°, and 70°). Error bars represent standard deviations.

$$\Delta p_i^t = p_i^t - p_i^0, \tag{3}$$

$$F^t = \sum_{i:\,\|\Delta p_i^t\| \geq \delta} \Delta p_i^t. \tag{4}$$

3) Frequency analysis of FT data and marker displacement

The sampling timestamps of the force–torque sensor data and the marker displacement data are not synchronized. Thus, both datasets were linearly interpolated to the uniformly spaced time-series data defined by the common sampling period $\Delta t = \frac{1}{f_s}$ as in equation (5), yielding discrete signals (6). Here, f_s denotes the lower of the two dataset's average sampling frequencies, t_0 the start time of the analysis interval, and N the number of samples generated.

$$t_n = t_0 + n\,\Delta t, \quad n = 0, 1, 2, \ldots, N-1 \tag{5}$$

$$\begin{aligned} \hat{F}_x[n] &= F_x(t_n), \\ \hat{M}[n] &= M(t_n) \end{aligned} \tag{6}$$

Subsequently, each resampled time series of $\hat{F}_x[n]$ and $\hat{M}[n]$ was smoothed using a Savitzky–Golay filter with a window length of 11 samples and a polynomial order of 3 ($\tilde{F}_x[n]$ and $\tilde{M}[n]$), and the power spectral density (PSD) in the 0–15 Hz range was computed using the Welch method (7).

$$S_{xx}(f_m) = \frac{1}{K\,U} \sum_{k=1}^{K} |\,\mathcal{F}\{\,w[n]\;\tilde{x}_k[n]\,\}(f_m)|^2 \tag{7}$$

The variables in (7) are defined as follows. $\tilde{x}_k[n]$ denotes the kth segment of the smoothed discrete-time signal $\tilde{x}[n]$, obtained with a segment length of $L = 256$ samples and a 50% overlap (128 samples). $w[n]$ is the Hann window applied to each segment. U is the window-power normalization factor, computed as $U = \frac{1}{L}\sum_{n=0}^{L-1} w^2[n]$. K represents the total number of segments used in the averaging process. f_m is the mth discrete frequency bin, given by $f_m = \frac{m f_s}{L}$, where f_s is the common sampling frequency of the resampled signals.

V. EXPERIMENTAL RESULTS

A. Contact area comparison result

This section presents the experimental results in a comparison of the contact area against a flat surface for w-VBTS and wo-VBTS configurations, using the four types of flexible skins (No. 1, No. 2, No. 4, and No. 5) listed in TABLE I. The results of the contact area analysis conducted using GIMP and converted to units of mm² according to equation (1) are presented in Fig. 7. For each condition, three contact angles of 50°, 60°, and 70° were tested, with ten measurements conducted for each angle. In the Fig. 7, the colored bars represent the mean values, while the black bars indicate the standard deviations. As can be seen, there is a clear difference in the contact area values between the w-VBTS

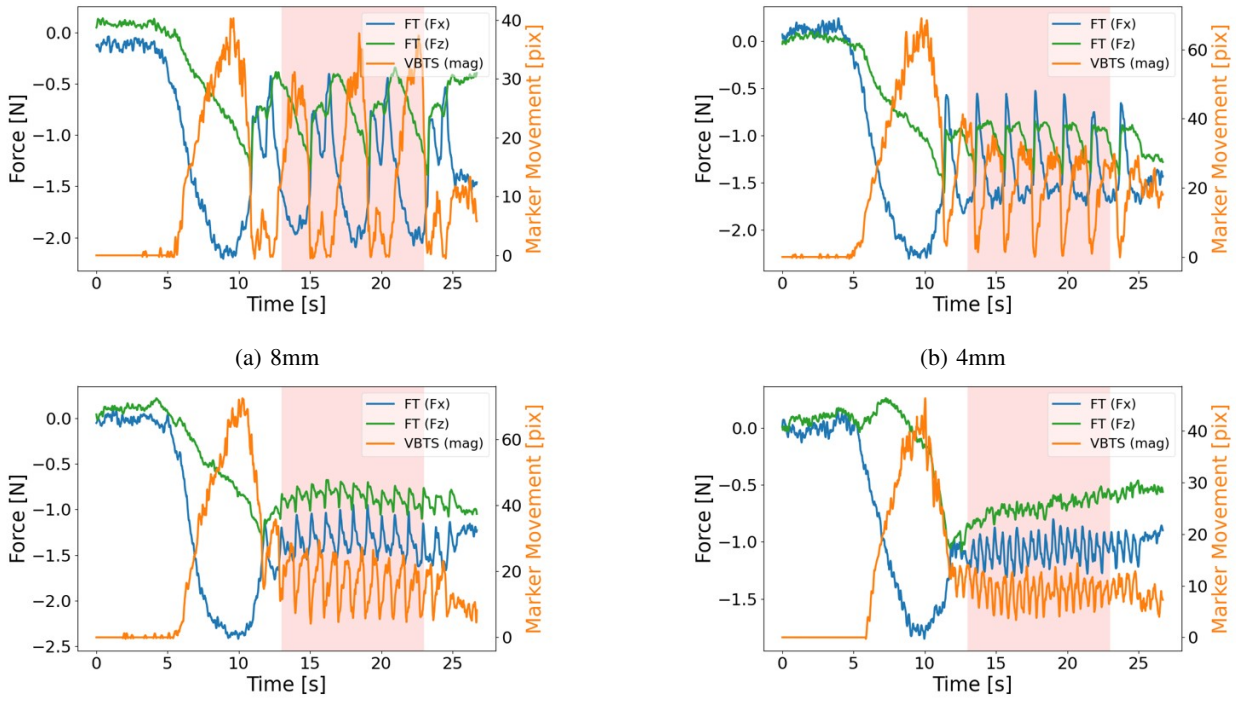

(a) 8mm

(b) 4mm

(c) 2mm

(d) 1mm

Fig. 8: Time-series plots of force (F_x,F_z) measured by the FT sensor and marker displacement magnitude from the w-VBTS (orange) during fine step detection experiments. Each subplot corresponds to a different step pitch d of the triangular ridged specimen: (a) $d = 8$ mm, (b) $d = 4$ mm, (c) $d = 2$ mm, and (d) $d = 1$ mm. The shaded regions indicate the time intervals where the sensor was in continuous contact with the steps.

TABLE II: Statistical comparison of contact areas between w/wo-VBTS for each material and contact angle.
WT : Welch's t-test, MWU : Mann–Whitney U test,
$*$: Significant after Bonferroni correction.

No.	Material	Angle	Test Used	p-value
1	Ecoflex	50°	WT	0.66
2	00-50	60°	WT	0.36×10^{-1}
3		70°	WT	$*0.3 \times 10^{-4}$
4	Ecoflex	50°	WT	$*0.18 \times 10^{-7}$
5	00-10	60°	WT	$*0.14 \times 10^{-2}$
6		70°	MWU	$*0.58 \times 10^{-3}$
7	Solaris	50°	WT	0.25×10^{-1}
8	and	60°	WT	0.52
9	Slacker	70°	WT	0.17
10	Gel	50°	WT	$*0.11 \times 10^{-12}$
11		60°	WT	0.15
12		70°	MWU	0.18

and wo-VBTS configurations using Ecoflex 00-10 across all three contact angle conditions. For the mixed material of Solaris and Slacker, the gel material, and Ecoflex 00-50, the contact area against the flat surface was larger for the w-VBTS than for the wo-VBTS in all conditions except for the 50° contact angle with Ecoflex 00-50.

The results of the statistical tests for these differences are shown in TABLE II. After applying a Bonferroni correction, statistically significant differences between the w-VBTS and wo-VBTS were retained for all contact angles with Ecoflex 00-10 (TABLE II, No. 4–6). In contrast, for the other skin materials, significance after correction was observed only in a subset of conditions and most comparisons did not reach the adjusted significance level. These results suggest, in line with previous studies [16] [18], that mimicking the human fingertip structure reproduces in Ecoflex 00-10 the role of limiting excessive skin deformation and further indicate that achieving an increased contact area through human finger inspired structures requires careful consideration of the material properties.

TABLE III: Comparison between ideal and measured PSD frequencies, and distance errors.

No.	d [mm]	Ideal [Hz]	PSD [Hz]	Distance Error [mm]
1	8	0.25	0.23	+0.6957
2	4	0.50	0.47	+0.2553
3	2	1.00	0.94	+0.1277
4	1	2.00	1.88	+0.0638

B. Texture detection evaluation result

This section presents the results of experimental evaluating the performance of the w-VBTS structure, using the proposed Solaris and Slacker mixed material as the skin, in detecting fine steps. The time-series graphs of the X-axis force variation from the force–torque sensor and the marker displacement of the w-VBTS, both smoothed using

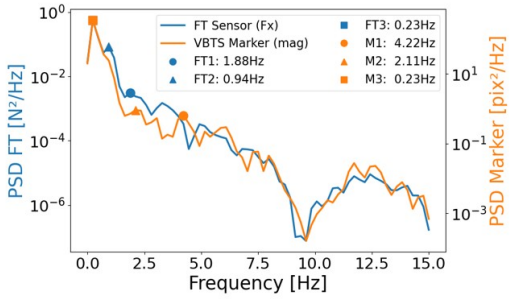

(a) 8mm

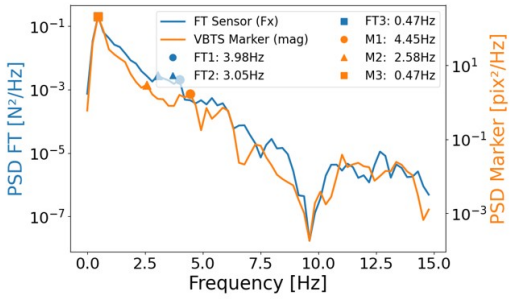

(b) 4mm

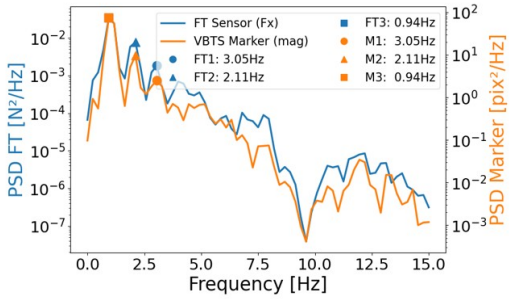

(c) 2mm

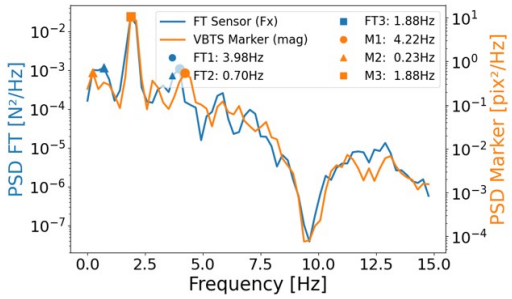

(d) 1mm

Fig. 9: Power spectral density (PSD) of force (F_x) measured by the FT sensor and marker displacement magnitude from the w-VBTS during fine step detection experiments. Each subplot corresponds to a different step pitch d: (a) 8 mm, (b) 4 mm, (c) 2 mm, and (d) 1 mm.

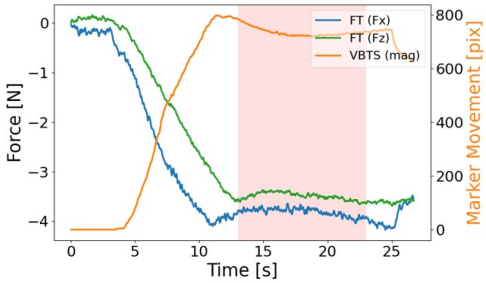

(a) wo-VBTS smoothed data ($d = 1$ mm)

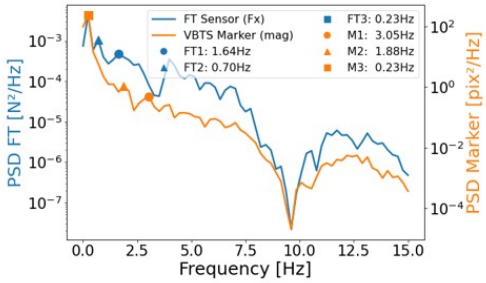

(b) wo-VBTS PSD ($d = 1$ mm)

Fig. 10: Time-series plots of force (F_x, F_z) and corresponding power spectral density obtained from the FT sensor and marker displacement magnitude during fine step detection experiments using the wo-VBTS.

equation (6), are shown in Fig. 8. It can be seen that the values obtained from the force-torque sensor (F_x) exhibit a similar trend to the marker displacement.

The results of the power spectrum density calculation (7) for the signals from 13 s to 23 s in these time series data are shown in Fig. 9 . In addition, TABLE III summarizes the ideal frequencies for the specimens (Fig. 6, d = 8, 4, 2, and 1 mm) and the PSD errors with respect to the peak values and the true values (mm) obtained from the PSD analysis. The measurement error was at most 0.69 mm for the specimen with $d = 8, 4, 2, 1$ mm, which indicates that the peak frequency obtained from the PSD analysis closely matches the ideal frequency.

Furthermore, in the experiments conducted with the wo-VBTS under the same conditions, the PSD analysis yielded peaks consistent with those obtained using the w-VBTS for specimens with step pitches ranging from $d = 8$ mm to $d = 2$ mm. However, for $d = 1$ mm, the ideal frequency of 2 Hz was not obtained (Fig. 10). Furthermore, Fig. 8 and 10 show that, in the case of the w-VBTS, fine step detection is achieved even though the normal force component (F_z) remains relatively low, indicating that the proposed design can effectively sense minute surface variations without requiring substantial normal loading.

These results demonstrate that incorporating the nail structure into the VBTS enables direct detection of fine steps at the nail tip.

VI. CONCLUSIONS

In this study, we designed a vision-based tactile sensor (VBTS) that mimics the structure of the human finger and conducted two evaluations. In the first evaluation, the contact areas on a flat surface were compared between w-VBTS and wo-VBTS using four flexible skin materials. Ecoflex 00-10 exhibited mechanical properties close to those of human skin and high shape conformability, similar to [16]. The nail structure in w-VBTS was found to suppress excessive skin deformation and increase contact area.

On the other hand, for the other flexible skin materials, no statistically significant difference in contact area due to the presence or absence of the nail structure was observed. These findings indicate that the material properties must be carefully selected in order to fully elicit the contact area enhancing effect of the nail structure.

In the second evaluation, w-VBTS with a flexible skin composed of a mixture of Solaris and Slacker was used to detect fine steps at the nail tip. PSD analysis confirmed direct detection on the specimen, with a maximum error of 0.69 mm. Additionally, for the specimen with a step pitch $d = 1$ mm, the w-VBTS successfully detected the ideal frequency with a normal force (F_z) of approximately -1 N, while the wo-VBTS required a normal force exceeding -3 N and still failed to detect the ideal frequency. These results suggest that, by concentrating the contact force at the nail tip, the nail structure played a significant role in enabling the detection of such fine steps.

Taken together, the comparative experiments on contact area and the experiments detecting fine steps at the fingertip demonstrate the effectiveness of mimicking the structure of the human finger in the sensor design of VBTS.

In future work, we plan to conduct experiments involving various objects, particularly thin planar objects, to further investigate the importance of mimicking the structure of the human finger.

ACKNOWLEDGMENT

This work was supported by JST SPRING, Japan Grant Number JPMJSP2102; also in part by the JST CREST program.

REFERENCES

[1] R. Johansson and J. Flanagan, "Coding and use of tactile signals from the fingertips in object manipulation tasks," *Nature reviews. Neuroscience*, vol. 10, pp. 345–59, 05 2009.

[2] C. Wang, L. Dong, D. Peng, and C. Pan, "Tactile sensors for advanced intelligent systems," *Advanced Intelligent Systems*, vol. 1, no. 8, p. 1900090, 2019. [Online]. Available: https://advanced.onlinelibrary.wiley.com/doi/abs/10.1002/aisy.201900090

[3] A. Schmitz, P. Maiolino, M. Maggiali, L. Natale, G. Cannata, and G. Metta, "Methods and technologies for the implementation of large-scale robot tactile sensors," *IEEE Transactions on Robotics*, vol. 27, no. 3, pp. 389–400, 2011.

[4] M. R. Kulkarni, R. A. John, M. Rajput, N. Tiwari, N. Yantara, A. C. Nguyen, and N. Mathews, "Transparent flexible multifunctional nanostructured architectures for non-optical readout, proximity, and pressure sensing," *ACS Applied Materials & Interfaces*, vol. 9, no. 17, pp. 15 015–15 021, 2017, pMID: 28422483. [Online]. Available: https://doi.org/10.1021/acsami.6b16840

[5] T. P. Tomo, A. Schmitz, W. K. Wong, H. Kristanto, S. Somlor, J. Hwang, L. Jamone, and S. Sugano, "Covering a robot fingertip with uskin: A soft electronic skin with distributed 3-axis force sensitive elements for robot hands," *IEEE Robotics and Automation Letters*, vol. 3, no. 1, pp. 124–131, 2018.

[6] C. Chorley, C. Melhuish, T. Pipe, and J. Rossiter, "Development of a tactile sensor based on biologically inspired edge encoding," in *2009 International Conference on Advanced Robotics*, 2009, pp. 1–6.

[7] R. Li, R. Platt, W. Yuan, A. ten Pas, N. Roscup, M. A. Srinivasan, and E. Adelson, "Localization and manipulation of small parts using gelsight tactile sensing," in *2014 IEEE/RSJ International Conference on Intelligent Robots and Systems*, 2014, pp. 3988–3993.

[8] B. Ward-Cherrier, L. Cramphorn, and N. F. Lepora, "Tactile manipulation with a tacthumb integrated on the open-hand m2 gripper," *IEEE Robotics and Automation Letters*, vol. 1, no. 1, pp. 169–175, 2016.

[9] B. Ward-Cherrier, N. Rojas, and N. F. Lepora, "Model-free precise in-hand manipulation with a 3d-printed tactile gripper," *IEEE Robotics and Automation Letters*, vol. 2, no. 4, pp. 2056–2063, 2017.

[10] N. Lepora, Y. Lin, B. Money-Coomes, and J. Lloyd, "Digitac: A digit-tactip hybrid tactile sensor for comparing low-cost high-resolution robot touch," *IEEE Robotics and Automation Letters*, vol. 7, pp. 1–7, 10 2022.

[11] S. Wang, Y. She, B. Romero, and E. Adelson, "Gelsight wedge: Measuring high-resolution 3d contact geometry with a compact robot finger," in *2021 IEEE International Conference on Robotics and Automation (ICRA)*. IEEE Press, 2021, p. 6468–6475. [Online]. Available: https://doi.org/10.1109/ICRA48506.2021.9560783

[12] P. Rayamane, Z. Ji, and M. Packianather, "Design and development of a robust vision-based tactile sensor," in *2022 IEEE/ASME International Conference on Advanced Intelligent Mechatronics (AIM)*, 2022, pp. 1417–1423.

[13] W. K. Do, A. Dhawan, M. Kitzmann, and M. Kennedy, "Densetact-mini: An optical tactile sensor for grasping multi-scale objects from flat surfaces," 05 2024, pp. 6928–6934.

[14] Y. Zhou, P. Zhou, S. Wang, and Y. She, "In-hand singulation, scooping, and cable untangling with a 5-dof tactile-reactive gripper," *Advanced Robotics Research*, vol. 1, 08 2025.

[15] D. A. R. De Berker, J. André, and R. Baran, "Nail biology and nail science," *International Journal of Cosmetic Science*, vol. 29, no. 4, pp. 241–275, 2007. [Online]. Available: https://onlinelibrary.wiley.com/doi/abs/10.1111/j.1467-2494.2007.00372.x

[16] M. Controzzi, M. D'Alonzo, C. Peccia, C. M. Oddo, M. C. Carrozza, and C. Cipriani, "Bioinspired fingertip for anthropomorphic robotic hands," *Applied Bionics and Biomechanics*, vol. 11, no. 1-2, p. 864573, 2014. [Online]. Available: https://onlinelibrary.wiley.com/doi/abs/10.3233/ABB-140092

[17] R. Shirato, A. Abe, H. Tsuchiya, and M. Honda, "Effect of fingernail length on the hand dexterity," *Journal of Physical Therapy Science*, vol. 29, pp. 1914–1919, 11 2017.

[18] A. Kumagai, Y. Obata, Y. Yabuki, Y. Jiang, H. Yokoi, and S. Togo, "Comparison of precision grasping performance between artificial fingers with and without nails," in *2022 IEEE 4th Global Conference on Life Sciences and Technologies (LifeTech)*, 2022, pp. 380–381.

[19] K. Murakami and T. Hasegawa, "Novel fingertip equipped with soft skin and hard nail for dexterous multi-fingered robotic manipulation," in *2003 IEEE International Conference on Robotics and Automation (Cat. No.03CH37422)*, vol. 1, 2003, pp. 708–713 vol.1.

[20] B. Romero, F. Veiga, and E. Adelson, "Soft, round, high resolution tactile fingertip sensors for dexterous robotic manipulation," in *2020 IEEE International Conference on Robotics and Automation (ICRA)*, 2020, pp. 4796–4802.

[21] D. F. Gomes, Z. Lin, and S. Luo, "Geltip: A finger-shaped optical tactile sensor for robotic manipulation," in *2020 IEEE/RSJ International Conference on Intelligent Robots and Systems (IROS)*, 2020, pp. 9903–9909.

[22] I. Andrussow, H. Sun, K. J. Kuchenbecker, and G. Martius, "Minsight: A fingertip-sized vision-based tactile sensor for robotic manipulation," *Advanced Intelligent Systems*, vol. 5, no. 8, p. 2300042, 2023. [Online]. Available: https://advanced.onlinelibrary.wiley.com/doi/abs/10.1002/aisy.202300042

[23] O. Azulay, N. Curtis, R. Sokolovsky, G. Levitski, D. Slomovik, G. Lilling, and A. Sintov, "Allsight: A low-cost and high-resolution round tactile sensor with zero-shot learning capability," *IEEE Robotics and Automation Letters*, vol. 9, no. 1, pp. 483–490, 2024.

[24] G. Jocher, A. Chaurasia, and J. Qiu, "Yolo by ultralytics," 2023, available from: https://github.com/ultralytics/ultralytics.